

Research Article

Working Mechanism of Pile Group with Different Pile Spacing in Dense Sand

Yadong Chen ¹, Fan Lu ², Abdoullah Namdar ¹ and Jiangdong Cai ¹

¹Faculty of Architecture and Civil Engineering, Huaiyin Institute of Technology, Huai'an 223001, China

²College of Transportation Science & Engineering, Nanjing Tech University, Nanjing 210009, China

Correspondence should be addressed to Yadong Chen; chenrundong2004@163.com

Received 26 April 2019; Accepted 24 June 2019; Published 4 July 2019

Academic Editor: Giovanni Garcea

Copyright © 2019 Yadong Chen et al. This is an open access article distributed under the Creative Commons Attribution License, which permits unrestricted use, distribution, and reproduction in any medium, provided the original work is properly cited.

Complex interaction mechanism exists between the pile group and soil. To realize the pile-soil load transmission mechanism in detail, the failure pattern of pile groups installed in dense sand considering different pile spacing was investigated by means of laboratory experimental model test and three-dimensional discrete element method. The results suggested that the narrow pile spacing was beneficial to the development of the pile tip resistance, and it enhanced the bearing performance of the pile group at the initial stage of settlement. The pile spacing changed the shaft resistance pattern with modification of the strain energy mechanism released within the subsoil. The pile group with $6b$ pile spacing had higher composite group efficiency. A joint fan-shaped displacement zone was formed beneath the pile tip for the pile group with $3b$ pile spacing; this pile foundation presented the block failure mechanism. The sand displacement beneath the cap for the pile group with $6b$ pile spacing mainly located on the upper part of the piles, the sand displacement around both sides of the piles presented asymmetric, and a relatively independent fan-shaped displacement zone was formed beneath the pile tip.

1. Introduction

Pile groups are widely used as a deep foundation to improve stability of the residential building, transmission tower, drilling platform, and several other types of infrastructure. Many researchers have been studying the bearing capacity, settlement, failure pattern, and transmission load mechanism of the pile group by means of theoretical analysis, model test, and numerical simulation, and they have also achieved considerable progress [1–3]. However, the pile group is a complex substructure system, and research on that involves many factors, such as load transfer, overall settlement, pile arrangement, and geological conditions. The pile group-soil interaction needs more scientific investigation by means of applying the theoretical concept, experimental, numerical simulation, or combination of different methods [4–6].

In studying pile group-soil interaction, considering the bearing capacity of soil and piles is closely related to the deformation of soil and piles and micromechanical properties of soil. The traditional methods of measuring soil deformation

are the punctuation method and grid method in the model test [7, 8], which are suitable for measuring large soil deformation. The number of observation points is limited, and the range of deformation measurement is local. In recent years, X-ray CT, particle image velocimetry (PIV), and digital image correlation (DIC) technology have been introduced to study the performance of a single pile and pile groups, which provides new ways for analyzing the bearing capacity and deformation behavior of pile foundation [9–11]. For example, the X-ray CT system was used to study the soil displacement field around open-ended pipe piles during penetration [12]. Synthetic transparent soil was adopted to visualize the pile-soil interaction, and the vertical and horizontal soil displacement caused by a sequence of jacked piles was discussed [13]. The influence of pile spacing on the bearing capacity of the pile group and the soil deformation near the pile tip was analyzed with the help of PIV technology [14, 15].

With the increase in computing power, the numerical simulation technology of the particle flow code based on the discrete element method (DEM) has been applied in the

study micromechanism of pile foundation. For example, Duan et al. [16] used the discrete element method to compare and analyze the bearing characteristics of cast-in-place piles and driven piles, and it has been found the different distribution patterns of shaft resistance and tip resistance and the driven pile presented a better bearing performance in the pile load test. El Shamy and Elmekati [17] adopted the DEM-FEM coupling method to simulate the load-settlement characteristics and load transfer mechanism of pile foundation. Zhou et al. [18] used PFC2D to study the micromechanical behavior of soil particles around piles and found that the mechanism of shaft resistance of piles in the pile group is different from the single pile.

However, in the existing literature, the research on the progressive development law of soil deformation under pile caps and between piles was insufficient. A two-dimensional discrete element model was only an approximate verification of the working characteristics of the pile group, and the internal mechanism of interaction between the pile group and soil has not been fully understood. In this paper, we designed a geotechnical test device and applied the non-contact deformation testing method to examine the bearing performance, sand displacement field, and shear strain field of pile groups with different pile spacing. The test results have been verified by a three-dimensional discrete element model, which was used to study the pile group's load transfer characteristics and sand stress change law.

2. Digital Image Correlation Technique

DIC is a typical pattern recognition and noncontact deformation measurement technique, which is used in particle image velocimetry, particle tracking, speckle velocimetry, and other experimental techniques [19]. A series of test images were acquired by the camera and converted into gray images. The gray images taken before and after soil deformation are segmented into many interrogations. The interrogation before deformation was matched with the gray image after deformation, and the position of the interrogation after deformation was determined according to the peak correlation coefficient; thus, the displacement of the interrogation can be obtained. The whole displacement field can be determined by performing similar operations on all interrogations. The DIC technique has been used by some researchers to measure soil deformation and successfully achieve reliable results in geotechnical engineering [20, 21]. The standard correlation function, C , was given as

$$C(\Delta x, \Delta y) = \iint I_0(x, y) I_1(x + \Delta x, y + \Delta y) dx dy, \quad (1)$$

where x and y are dimensions in the interrogating area and I_0 and I_1 are the gray-scale intensities of the two images being compared (Image 0 and Image 1, respectively).

The accuracy of the DIC technique is controlled by the pixel resolution of the digital camera and the subpixel calculating method. Subpixel accuracy can be achieved via a Gaussian fit to the region closest to the peak. The details of this analysis technique can be found in [11, 22, 23]. In this

study, the DIC technique, programmed via the MATLAB procedure, was used to calculate sand displacement during the loading process. The smallest interrogation window size used in this analysis was 64 pixels by 64 pixels to obtain more displacement field data. In order to verify the reliability and accuracy of the DIC technique, the sand image was captured, and it was artificially shifted 3 pixels in horizontal and vertical directions, and then the image displacement before and after shifting was calculated by the DIC program. The statistical results showed that the average displacement was 2.938 pixels and the standard deviation was 0.022 pixels. The calculated results were in good agreement with the migration values.

Pixel displacement needs to be converted into model space displacement. Fixed marker points were set on the front frame of the container along with the horizontal and vertical directions, the pixel values occupied by adjacent marker points can be obtained, and then the actual length of each pixel can be deduced. In this experiment, the distance between horizontal marker points was 1000 mm, and the corresponding number of pixels was 3144, so the corresponding conversion ratio was 0.318 mm/pixel.

Based on the concept of a quadrilateral element, a calculation method based on the displacement mode is presented to determine the strain at the center of the elements [24, 25], and the maximum shear strain γ_{\max} is calculated using the following equation:

$$\gamma_{\max} = \sqrt{(\varepsilon_x - \varepsilon_y)^2 + \gamma_{xy}^2}, \quad (2)$$

where ε_x and ε_y are the strain components in the direction of X and Y , respectively, and γ_{xy} is the shear strain.

3. Experimental Setup and Testing Procedure

3.1. Similarity Ratio Design. For the static model tests, the main similarity indexes are geometric similarity, stress similarity, strain similarity, displacement similarity, Poisson's ratio, bulk density, boundary condition similarity, etc. It is almost impossible to satisfy all the above similar conditions, especially the similar conditions of the failure mechanism of a test. Generally, the main similar indexes are satisfied, while the requirements for other indexes are relaxed. In this model test, the similarity requirements of the model and the prototype are geometric similarity, boundary condition similarity, and main physical parameters' similarity. In this paper, local sand is used as model soil and concrete is used as the model pile material. According to the similarity theory, the geometric similarity ratio is 1 : 20. The material similarity such as gravity, internal friction angle, and modulus of elasticity is 1 : 1, and dimensionless parameters such as strain and Poisson's ratio are 1 : 1.

3.2. Experimental Setup. The experimental setup in this research consisted of a model container, loading frame, data acquisition system, digital camera, and computer, as shown in Figure 1. The transparent container had an inner dimension of 1000 (length) \times 1000 (width) \times 1000 (height)

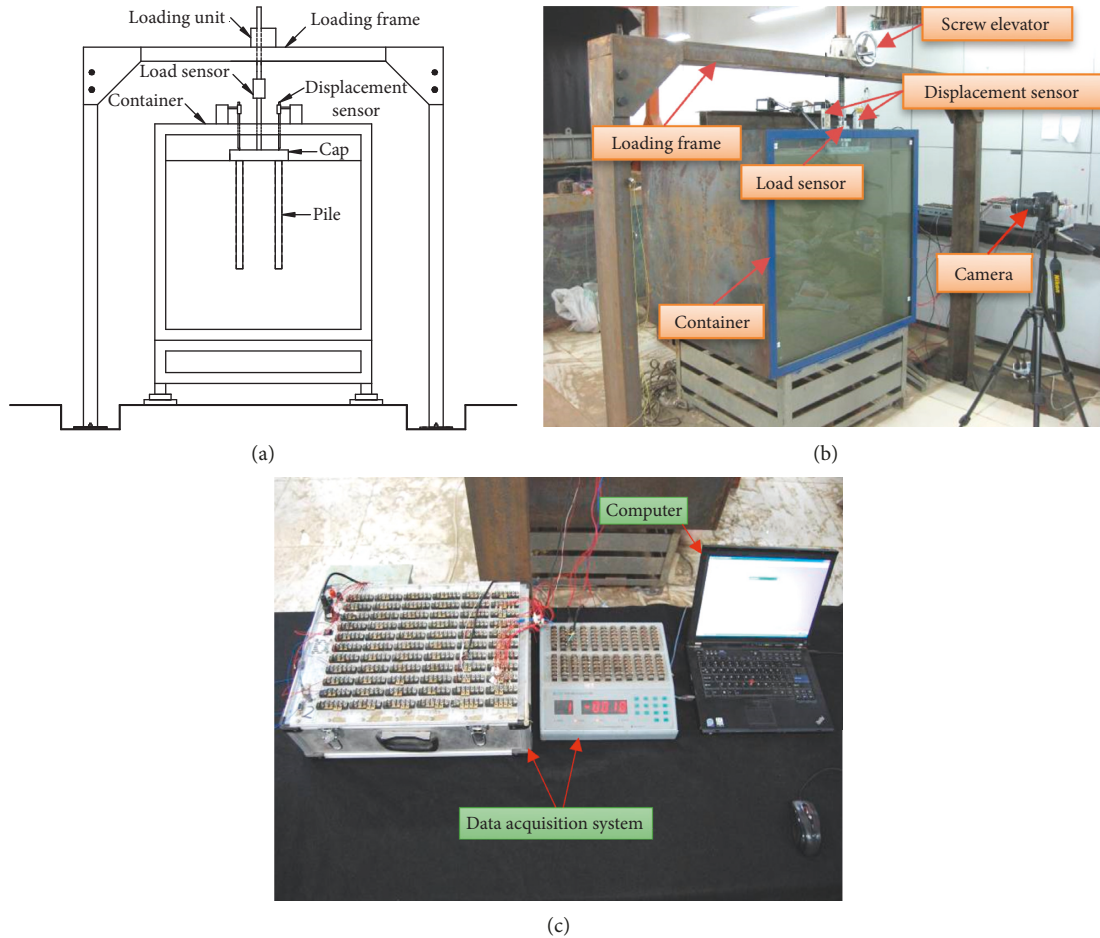


FIGURE 1: Test setup. (a) Schematic diagram of the test apparatus. (b) Model container and reaction frame. (c) Data acquisition system.

mm, with a toughened glass viewing window along one long side permitting to study sand displacement; thus, it is possible to observe the deformation process [22, 26]. In order to create a rigid boundary condition, the tempered glass with a thickness of 36 mm was fixed reliably with the container through a limit device. The other three sides and the bottom of the container were welded with steel plates, and the thickness of the steel plate was 10 mm. Therefore, in this paper, the influence of container deformation on test results was not to be considered. Although the tempered glass was smooth, there was indeed friction between glass and soil. Referring to the test methods, Teflon sheet and silicone oil can reduce the friction between soil and glass [14, 27]; in this test, a layer of silicone oil was coated on the glass surface to minimize the effect of interfacial friction on the displacement of sand particles.

The loading frame was used to apply the vertical load to the pile groups, consisting of a screw elevator and a load sensor with a maximum loading capacity of 50 kN. The load sensor was connected to the screw elevator through bolts, and the lower part of the load sensor was contacted with the cap through a spherical hinge. Two electronic displacement sensors with a resolution of 0.025 mm were symmetrically arranged on the top of the cap, and their average values were taken as the basic settlement values. The static resistance

strain indicators of DH3818 and DH3816 were combined to record the vertical load and settlement data. The digital camera, with a resolution of 3872×2592 pixels, from Nikon in Japan, was set up to take a series of images of the sand beneath caps while applying the load.

The model square pile was composed of fine stone concrete (C30), with a side length (b) of 30 mm and a length (L) of 600 mm. The cap was made from a steel plate with a thickness of 50 mm, and piles and caps were connected by embedded parts. As suggested by Arshad et al. [28] and Houda et al. [29], a pile installation was a vertically symmetrical process, and a semimodel pile group installation yields an equally accurate result. Semimodel pile groups with $3b$ and $6b$ pile spacing were buried in the sand soil as a bored pile foundation [18, 29] and placed against the tempered glass of the model container, as shown in Figure 2.

3.3. Sand Properties. Dry sand ($D_{50} = 0.63$ mm) was used in these laboratory experiments; the size distribution curve is provided in Figure 3. As suggested in [14, 18, 26], the model sand was layered into the container, and the weight of sand for each layer was calculated according to the relative density, maximum void ratio, minimum void ratio, specific gravity, and volume of each layer. The light compactor was used to tamp the sand repeatedly until the sand surface

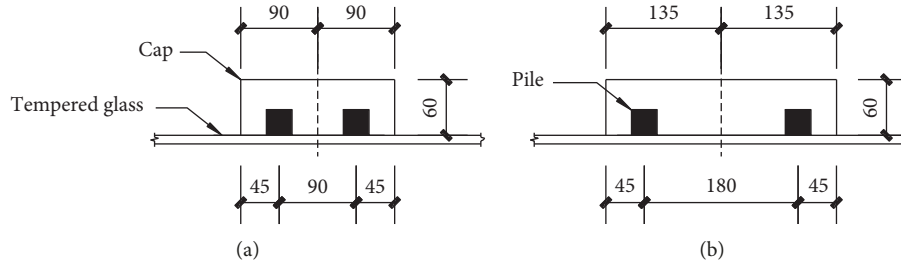


FIGURE 2: Plan view of the pile groups. (a) $3b$ pile spacing. (b) $6b$ pile spacing.

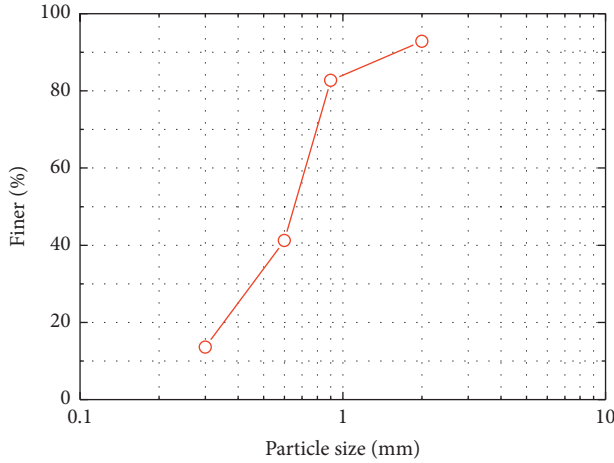


FIGURE 3: The size distribution curve of sand.

reaches the design height. The dry sand was found to give sufficient texture to permit measurement of the soil deformation via the DIC technique [30]. The physical properties of the sand are summarized in Table 1.

As suggested in [31–33], when the pile diameter was 20 times greater than the average soil size, the distance between the pile side and the rigid boundary was greater than 10 times the diameter of pile, and the influence of boundary condition on test results was acceptable. The ratio of pile width to D_{50} was 48, and the ratio of the model container width to pile width was 16.7, which are in agreement with the dimension conditions used in many previous experimental studies. In addition, the least boundary effect was confirmed in the subsequent displacement field test results.

3.4. Testing Procedure. The embedment depth of model piles was 600 mm from the pile tip to the ground surface. The sand was filled into the container layer by layer. When the sand was built up below the bottom of the piles, the model piles were placed on the surface of sand and close to the tempered glass and fixed with horizontal support; subsequently, the verticality of the model piles was controlled by a hammer and a horizontal ruler. Continue layered filling, and after filling to the top of the model piles, the cap and the piles were firmly connected. After standing for a period of time, it entered the stage of loading and collecting digital images.

First, the digital camera was located approximately 500 mm away from the model container, with its optical axis

TABLE 1: Physical properties of sand.

Property	Value
ρ	1650 kg/m ³
φ	32.5°
e_{\max}	1.14
e_{\min}	0.62
D_r	0.81
G_s	2.70

perpendicular to the container. The digital camera was set to the manual mode and controlled by a teleequipment [32], and the focal length and light source were then adjusted to obtain the best image quality. Second, the data acquisition system was connected to the PC and activated. Third, the pile group was pressed into the sand by manually turning the screw elevator, the loading mode was deformation control [18, 34], and the loading rate was 0.2 mm/min. Finally, a series of digital images, compressive loadings, and settlement data were captured by the camera and PC at each stage of settlement. Digital images captured from the test site are shown in Figure 4.

4. Analysis of Experimental Results

4.1. Load-Settlement Curves. The load-settlement curves of pile groups with different pile spacing are shown in Figure 5, where Q and S are the load and settlement on the cap, respectively. When the settlement S is less than 3.6 mm, the load-settlement curves of pile groups are almost overlapping, which indicates that the change of pile spacing at the initial stage of settlement has little effect on the bearing capacity of the pile foundation. After the settlement S exceeds 3.6 mm, the load-settlement curves begin to bifurcate. When the settlement is $S = 10$ mm, the load on the caps with $3b$ and $6b$ pile spacing is 7.77 kN and 8.79 kN, respectively, and the bearing capacity of the pile group with $6b$ pile spacing is obviously higher than that with $3b$ pile spacing. With the increase in the settlement, the bearing capacity of the pile group with $6b$ pile spacing increases faster than the pile group with $3b$ pile spacing, and the pile foundation has more slow-drop behavior.

4.2. Displacement Field Maps. The development of the displacement field can reflect the progressive failure process of the pile group. The displacement field of the pile group

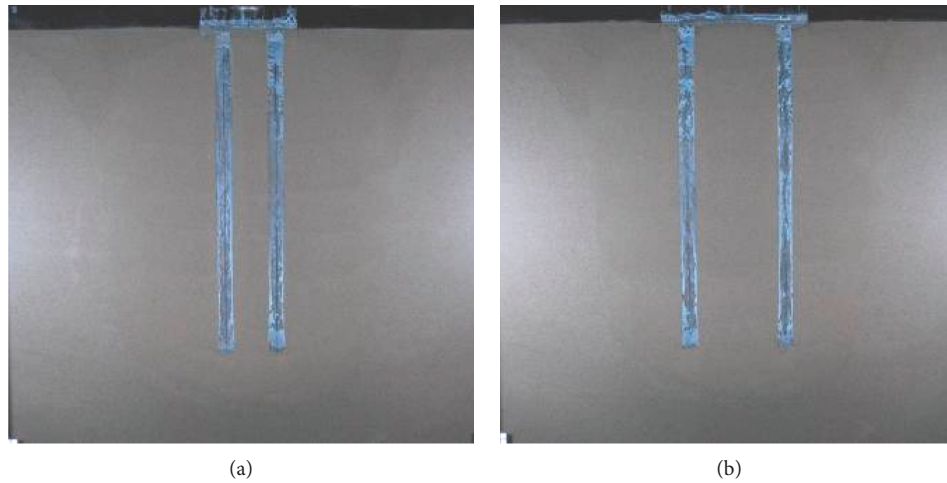


FIGURE 4: In situ images of the pile groups. (a) 3b pile spacing. (b) 6b pile spacing.

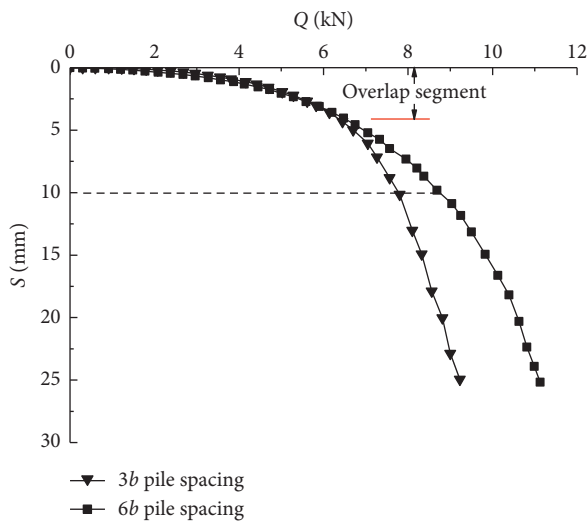


FIGURE 5: Load-settlement curves of pile groups.

with 3b pile spacing is shown in Figure 6 under four settlement stages: $S = 1.9225, 4.9850, 10.15,$ and 20.0375 mm, respectively. From the graph, it can be seen that in the initial stage of settlement, the sand displacement inside and outside of the piles is mainly vertical downward, but the sand displacement inside of the piles is larger than the outside of the piles. When $S = 4.9850$ mm, the horizontal displacement appears outside the pile tip and at the cap corner, but the value is small, and the sand displacement inside the piles remains vertical downward and unchanged. With the further increase in the settlement, the sand displacement below the pile tip and outside the piles is more obvious.

In the final settlement stage, due to the smaller pile spacing, the larger interaction exists between piles and sand, the sand movement is restricted by the piles, and the sand between piles is derived along the vertical direction. The sand displacement beneath the pile tip presents a fan-shaped distribution as shown in Figure 6(d), which is inconsistent with the traditional soil deformation mode proposed by Meyerhof [35]. In addition, the fan-shaped distribution area

overlaps on the inner side of the pile tip, and the sand displacement in the overlap area is vertical and downward, and the stress overlap makes the horizontal component of the sand displacement disappear.

The displacement field of the pile group with 6b pile spacing is shown in Figure 7 under four pile-settlement stages: $S = 2.055, 5.2075, 9.805,$ and 20.3125 mm, respectively, and the development of the displacement field is different from the pile group with 3b pile spacing. When $S = 2.055$ mm, the sand displacement around the piles is mainly vertical and downward, and the displacement mainly occurs near the pile tip. When $S = 5.2075$ mm, the lateral sand displacement beneath the pile tip increases, and the vertical sand displacement between the piles gradually develops to the deep part of the sand. When $S = 9.805$ mm, the sand displacement outside the pile is mainly inclined downward, and the sand displacement beneath the pile tip presents the displacement pattern of cavity expansion [36], similar to a single pile, but the sand displacement between the piles is mainly vertical downward. This phenomenon is observed in dense sand, even when the pile spacing has reached 6b, and the working behavior of piles is different from a single pile.

At the final settlement stage, the sand displacement beneath the pile tip in the pile group with 6b pile spacing is larger than 3b pile spacing; it reveals that the cap and pile-pile interaction have less restriction on the sand displacement at the pile tip in the pile group with 6b pile spacing, and the sand displacement beneath the pile tip presents a relatively independent fan-shaped distribution (Figure 7(d)). Large lateral displacement appears on the surface of model sand and outside of the piles. The sand displacement under the cap decreases rapidly along the sand depth direction, and the influence area of sand displacement could not extend below the pile tip.

4.3. *Displacement Contours.* We have plotted the displacement field maps into the displacement contours, as shown in Figure 8, to gain further insight into sand motions. These figures show the horizontal and vertical sand displacement

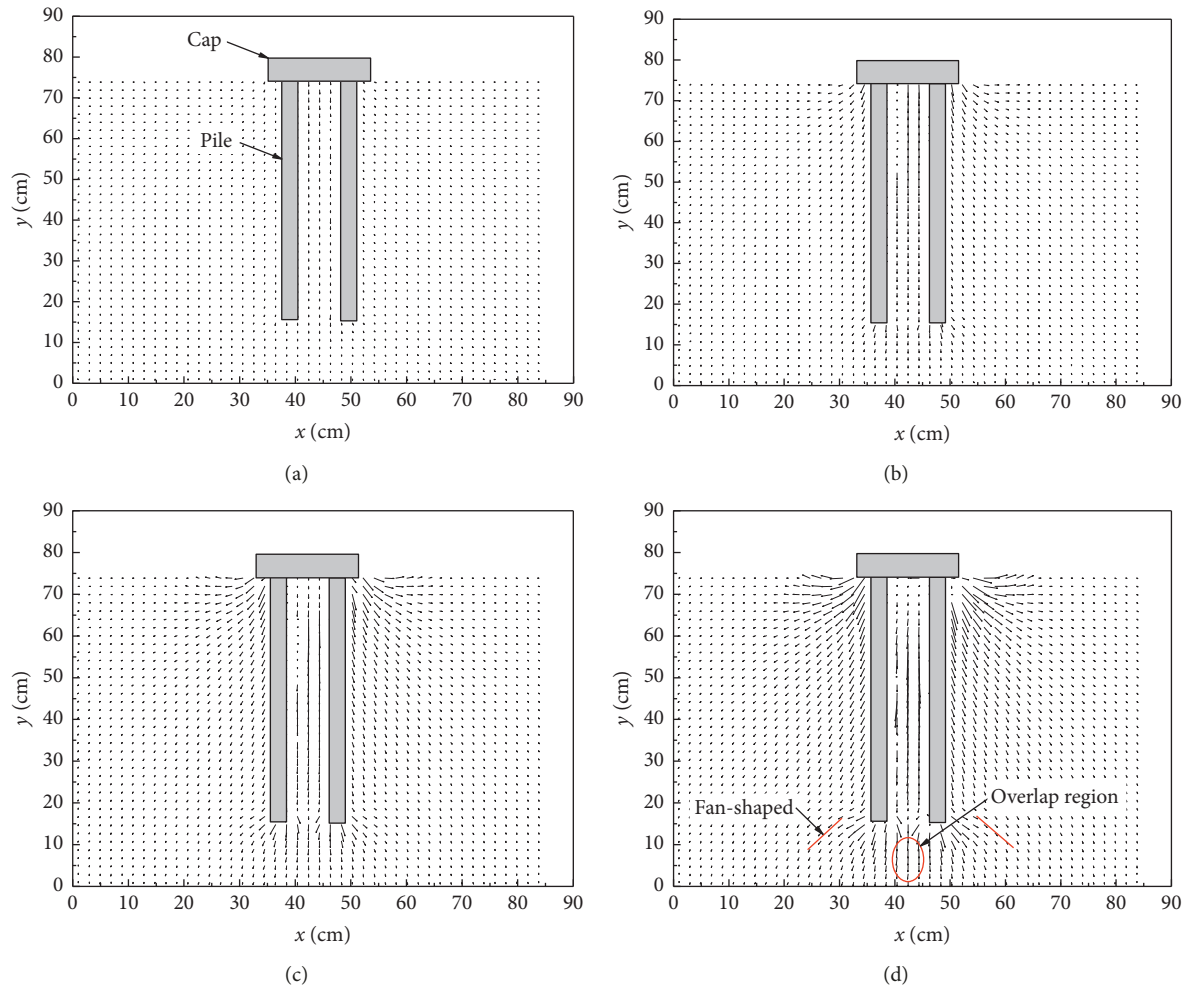


FIGURE 6: Soil displacement field of the pile group with $3b$ pile spacing. (a) $S = 1.9225$ mm. (b) $S = 4.9850$ mm. (c) $S = 10.15$ mm. (d) $S = 20.0375$ mm.

contours surrounding the pile group with $3b$ pile spacing at the final settlement stage; the contours were drawn at 0.2 mm intervals. Small pile spacing restrains the sand displacement between piles, which makes the horizontal sand displacement approach zero. The sand vertical displacement between piles decreases gradually along the pile length, which indicates that there is still an obvious relative displacement between the piles and sand. This phenomenon enhances pile friction resistance and increases pile displacement. A horizontal displacement bubble is formed in the sand outside the pile tip, and a joint vertical displacement bubble is formed in the sand below the pile tip. This phenomenon indicates that the displacement mechanism at the pile group is obviously different from a single pile [33].

From Figure 9, it can be seen that the vertical displacement is dominant in the sand between piles, and the horizontal displacement component is reached close to zero. The influence range of displacement is mainly concentrated on the upper sand layer ($4/5L$). The holding effect between adjacent piles still exists, while the horizontal displacement component of sand outside piles is relatively significant, which makes the distribution characteristics of sand

displacement inside and outside piles, and they are different from the single pile. The relatively complete horizontal and vertical displacement bubbles form beneath the pile tip, and the displacement mode of the sand beneath the pile tip is similar to the single pile (Figure 10).

4.4. Shear Strain Field. The maximum shear strain distribution is related to the formation and development of the shear slip surface [24, 26]. Distribution of the maximum shear strain field around pile groups with different pile spacing at the final settlement stage is shown in Figure 11. For the pile group with $3b$ pile spacing, the maximum shear strain is mainly concentrated in the sand located outside the piles, exactly between the piles and beneath the pile tip; it reveals the failure mode of a solid deep foundation [14]. Distribution shear strain field around piles is obviously different from the single pile [33], which is mainly manifested by the inconsistency of shear strain distribution inside and outside of the piles; it leads to develop the difference friction distribution mechanism inside and outside the piles. The shear strain bubbles under the pile tip coincide

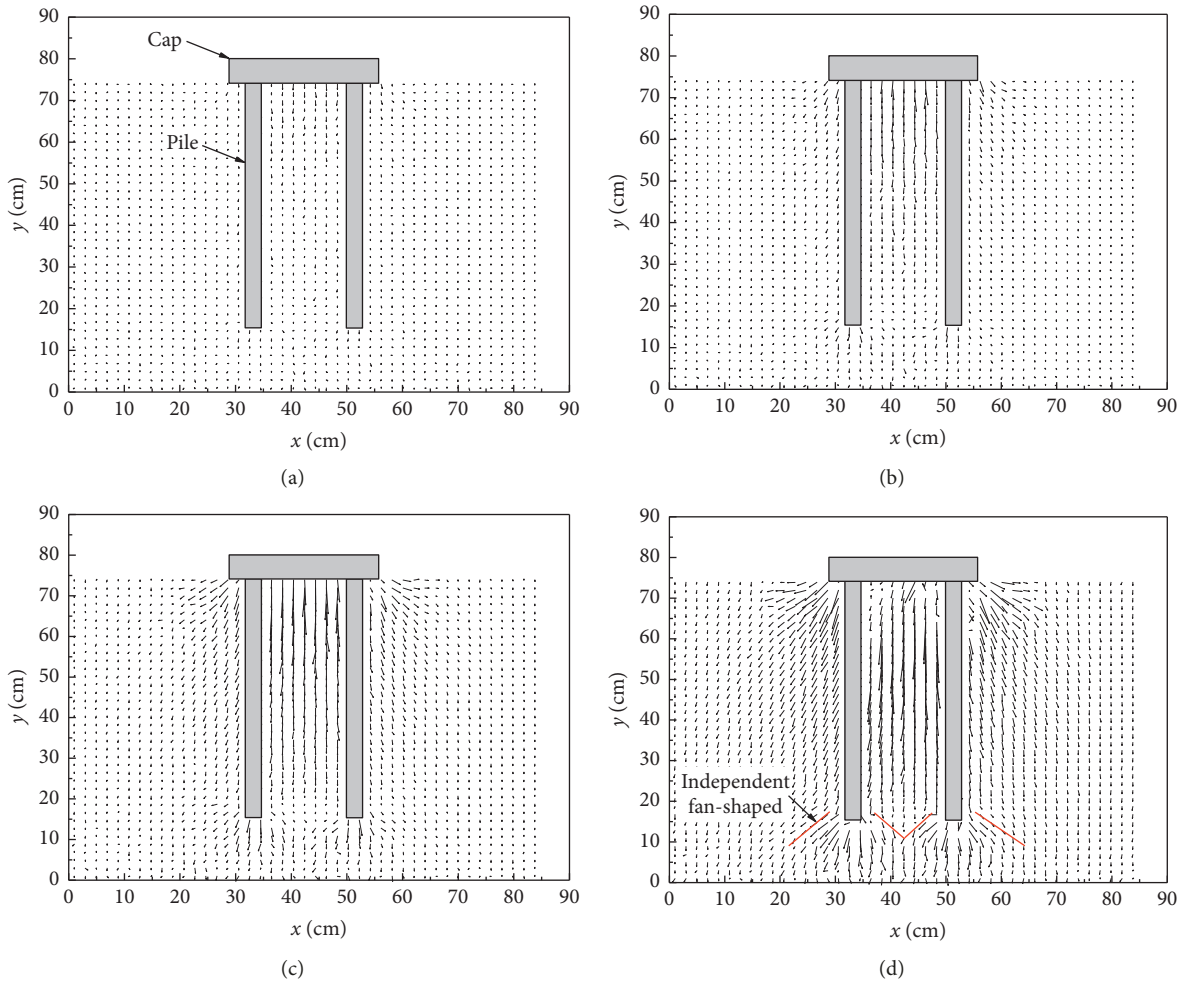


FIGURE 7: The sand displacement field of the pile group with $6b$ pile spacing. (a) $S = 2.055$ mm. (b) $S = 5.2075$ mm. (c) $S = 9.805$ mm. (d) $S = 20.3125$ mm.

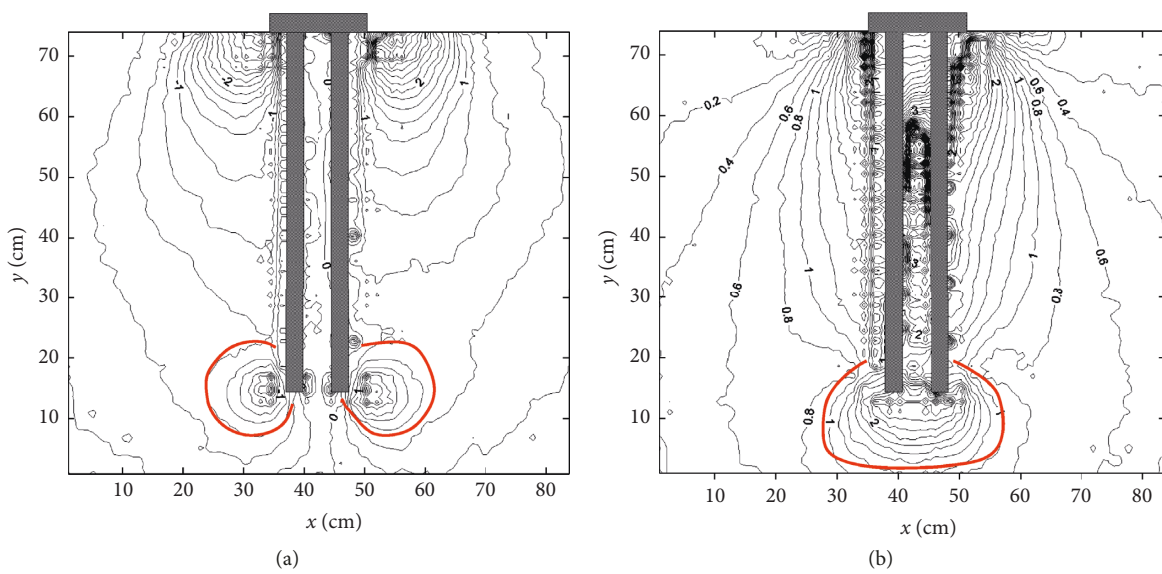


FIGURE 8: Displacement contour of the pile group with $3b$ pile spacing. (a) Horizontal displacement. (b) Vertical displacement.

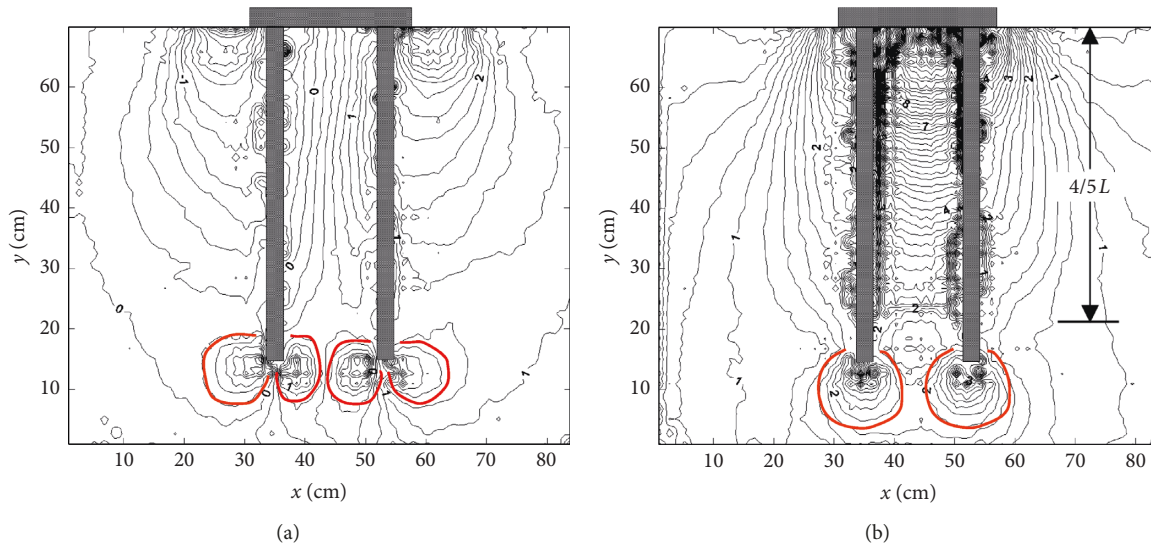


FIGURE 9: Displacement contour of the pile group with $6b$ pile spacing. (a) Horizontal displacement. (b) Vertical displacement.

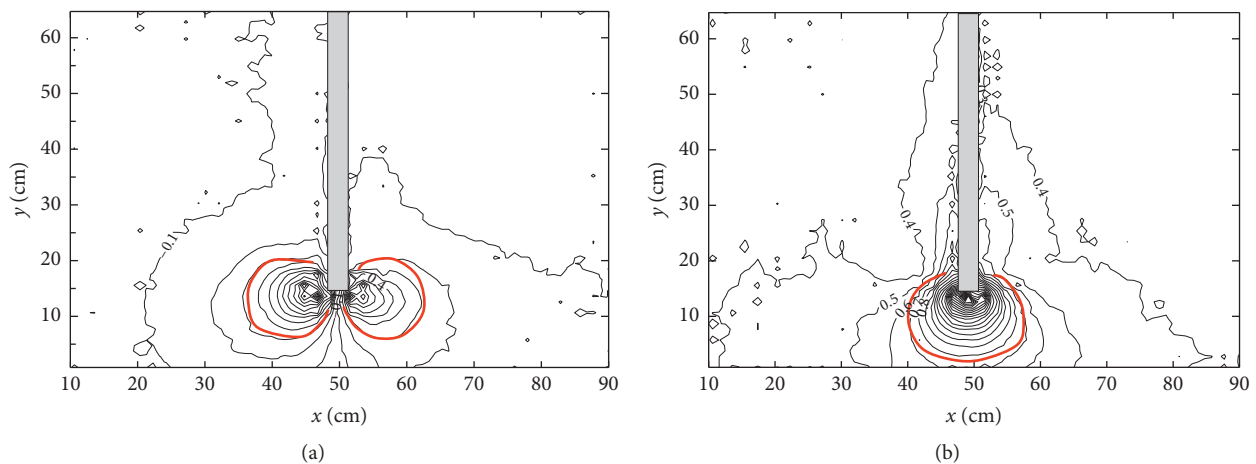


FIGURE 10: Displacement contours of the sand around a single pile. (a) Horizontal displacement. (b) Vertical displacement.

with each other, so it can be inferred that the stress overlap under the pile tip is serious.

The shear strain bubbles under the pile tip form independently at the pile group with $6b$ pile spacing, which is similar to a single pile, and the continuous strain bubbles (shown in red area) are formed under the cap. Two different strain energies are released which are observed in the pile group with $3b$ and $6b$ pile spacing; the pile arrangement is responsible for the strain-displacement mechanism.

5. DEM Simulation

The three-dimensional particle flow code (PFC3D) was developed by Itasca and based on the DEM [37, 38]; it was used to simulate the physical model experiment process for understanding pile group-sand interaction at a microscopic level.

The DEM simulation objects were two 2×2 model pile groups; they were in the symmetric stress state. From the

model symmetry conditions, only one-quarter of the model pile groups were represented [39]. A virtual model container was constructed with dimensions of 400 (length) \times 400 (width) \times 800 (height) mm replicating the model test setup. The virtual model container takes a smaller dimension to attain simulation efficiency. The dimension optimization helps eliminate peripheral particles which contribute at a minimum level. The boundaries are determined based on the model test results where the particles outside the 0.4 m width or 0.8 m depth barely move.

5.1. Micromechanical Parameter Identification. Sand particles were simulated using spherical balls. The particle size followed the uniform distribution, and the ratio of the largest radius to the smallest was 1.5. Particles with radius ranging from 4 to 6 mm were generated at a porosity of 0.42 under the gravity deposition method [40] (Figure 12(a)). The particle radius was magnified in PFC in order to improve

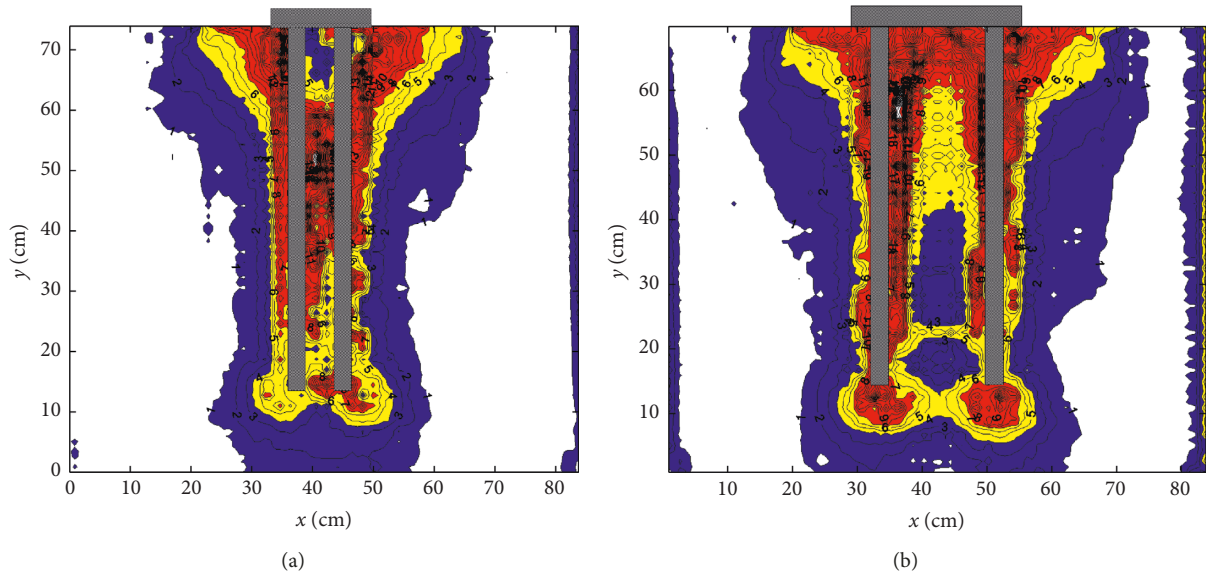


FIGURE 11: Contours of the maximum shear strain around the pile groups. (a) $3b$ pile spacing. (b) $6b$ pile spacing.

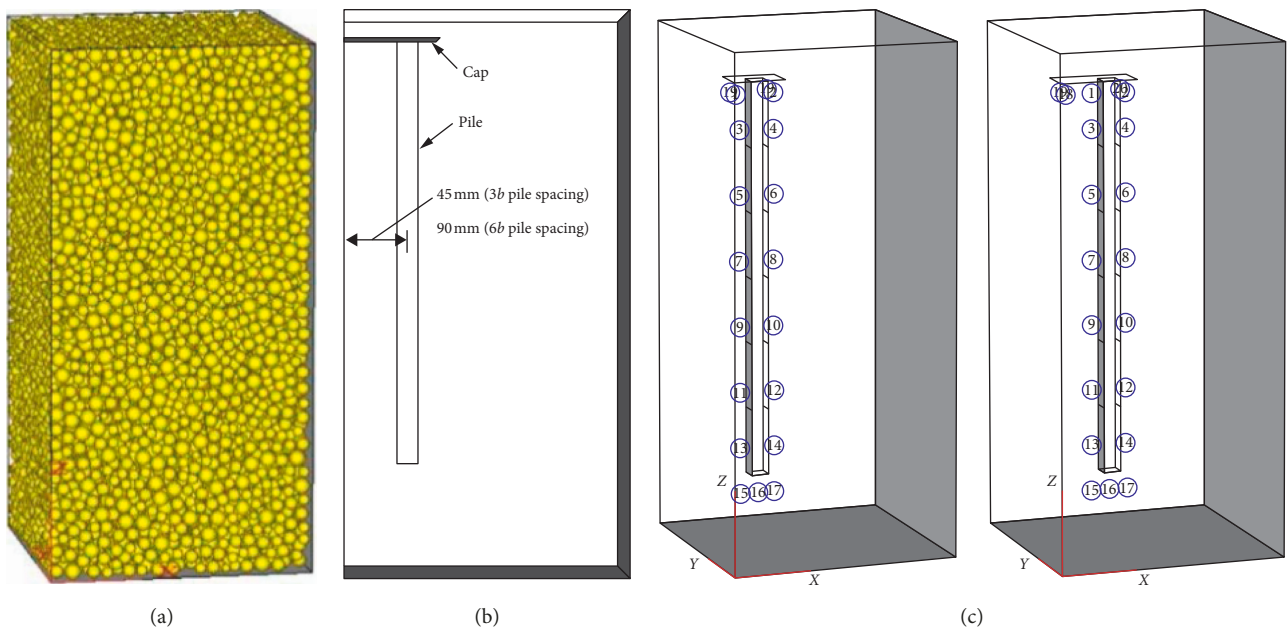


FIGURE 12: PFC3D model of the pile group and the layout of measurement spheres. (a) Sand model. (b) Distance between the pile to wall. (c) Measurement spheres.

computing efficiency. The relative sizes between the pile and the ball have been changed. As suggested in other similar PFC studies [41, 42], similar particle radius magnification was applied in this current study, and the particle size effect was accounted for calibrating micromechanical properties properly.

The pile group can be modeled by the particles with parallel bonds, which can apply load and simulate pile displacement; the simulation of the pile group needs to set appropriate parallel bond parameters [43]. The pile group also can be modeled by walls in numerical simulation, which are defined as a rigid flat entity in the PFC code [18];

the research results show that the walls can simulate the mechanical properties of piles [43, 44]. In the laboratory experiments, the square pile model was composed of fine stone concrete, which can be considered as rigid piles; the steel plate was chosen for the material of the model cap; the piles and the cap were fixed by connectors. Therefore, in the DEM modeling process, a number of vertical and horizontal parallel walls were used to form piles and the cap, which were connected as a whole to form rigid pile groups. A portion of the particles was deleted to accommodate the pile groups, and the pile dimension and the distance to wall boundary were the same as in the

laboratory experiments (Figure 12(b)). The load can be achieved by applying uniform velocity to the multifaceted wall of the pile group [45, 46]. The measurement spheres were used to calculate the average vertical stress and porosity at different stages of the simulation (Figure 12(c)).

The linear contact stiffness model was used to simulate the particle-particle and wall-particle interactions, which has been proved to simulate the interaction between the pile and sand [45, 47]. The input micromechanical parameters for the DEM simulation can be calibrated by biaxial, direct shear test or model test [40, 41, 48]. In this study, the pile loading test result was used to calibrate these micromechanical parameters. The bearing capacity of the pile group was the sum of the vertical contact forces of all the walls [49]. With reference to similar studies [42, 50], iterations were attempted to harmonize the simulation Q - S curve with the test curve, enabling material micromechanical parameter optimization. Q - S is often used to optimize the parameters of numerical simulation in similar DEM simulation of the pile foundation, and it has been proved that the results of parameter optimization can simulate the vertical compression characteristics of the pile foundation. The Q - S curves of pile groups with $3b$ and $6b$ pile spacing showed a reasonable agreement between the numerical simulation and experimental test (Figure 13). There are minor gaps between numerical simulation and model test curves, which mainly arise from the DEM model to stabilizing the simulation of interest.

Figure 14 is the soil displacement field distribution of the pile group with $3b$ pile spacing obtained by numerical calculation, which is basically consistent with the displacement pattern of soil around piles in the model test (Figure 6(d)). It further verifies the stability and accuracy of the mesoparameters. The optimized micromechanical parameters are presented in Table 2.

5.2. Numerical Simulation Results

5.2.1. Load Transfer Characteristics.

The load-settlement curves of pile groups with different pile spacing obtained by means of numerical simulation are shown in Figure 15. Q_s is the load shared by the sand under the cap and Q_p is the load shared by piles. When the settlement S is less than 5 mm, the bearing capacity of piles increases more than 60% and piles transfer most of the initial applied load, which indicates that the bearing capacity of piles is brought into play first. When the settlement S exceeds 5 mm, the load-sharing ratio of the piles with $3b$ pile spacing is always higher than the load shared by the sand under the cap, while the load-sharing ratio of the piles with $6b$ pile spacing almost coincides with the sand under the cap, and the bearing capacity of the piles and the sand is exerted simultaneously. After the settlement S exceeds 15 mm, the load shared by piles in the pile group with $3b$ pile spacing increases considerably; this is due to the larger pile-sand interaction caused by small pile spacing, which enhances the binding force of lateral extrusion of the sand between piles and beneath the pile tip, and thus has a beneficial effect

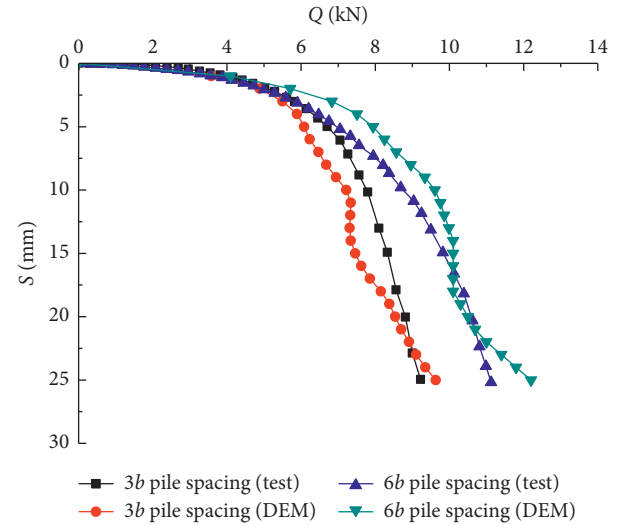


FIGURE 13: Comparison of numerical and experimental results.

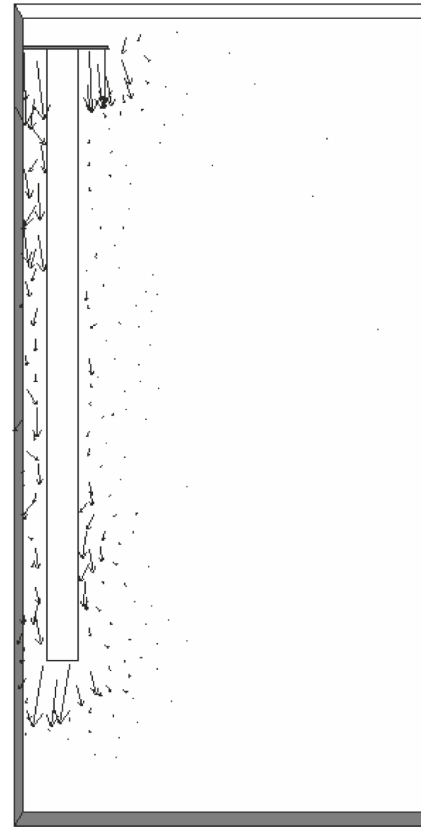
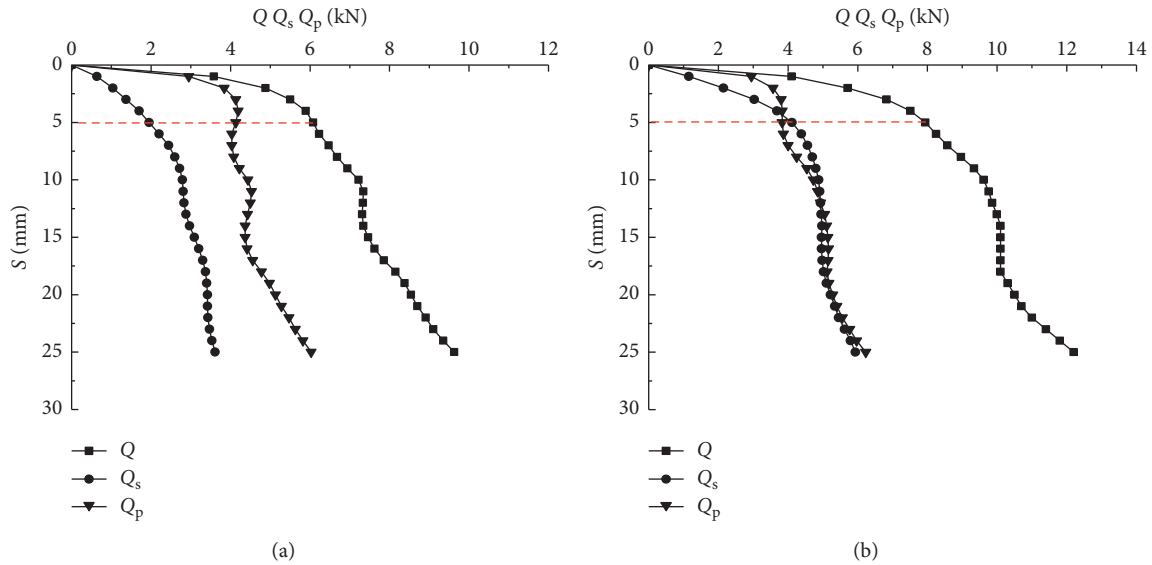


FIGURE 14: The soil displacement field of the pile group with $3b$ pile spacing in the DEM simulation.

on the increase in shaft resistance and tip resistance of piles in the later stage of the settlement. In the final settlement stage, the load-sharing ratios of piles and sand under the cap are 63% and 37%, respectively, in the pile group with $3b$ pile spacing and 51% and 49%, respectively, in pile group with $6b$ pile spacing, indicating that the load-sharing ratio of the sand under the cap increases obviously with the increase in pile spacing.

TABLE 2: Micromechanical parameters for the DEM simulation.

Parameter	Value
<i>Sand</i>	
Density	1650 kg/m ³
Particle number	17732
Smallest particle radius	4 mm
Largest particle radius	6 mm
Normal and shear stiffness	73 kN/m
Friction coefficient	0.7
<i>Pile group</i>	
Normal and shear stiffness	73 kN/m
Contact friction coefficient	0.7

FIGURE 15: Load-settlement curves of pile groups. (a) $3b$ pile spacing. (b) $6b$ pile spacing.

The variation curves of the internal and external shaft resistance of piles are shown in Figure 16; the internal shaft resistance and external shaft resistance of the pile were obtained by exporting the vertical force from the inner and outer wall of the pile and then dividing it by the area of the wall; average shaft friction was obtained by summing up the vertical forces of the four walls that make up the piles and dividing them by the total area of the walls. In the initial stage of the settlement, the shaft resistance of piles increases rapidly, and then the rate decreases significantly, which indicates that the shaft resistance of piles first exerts. For the pile group with $3b$ pile spacing, the internal shaft resistance of piles is about 1.5 times the external shaft resistance. This is mainly due to the large normal stress and releases strain energy on the internal surface of the pile caused by cap pressure transfer and pile-pile interaction, which improves the internal shaft resistance of piles.

When the pile spacing reaches $6b$, the difference of shaft resistance between the internal and external surface of the piles is obviously reduced, and it tends to be the same in the final settlement stage. It is noteworthy that the average shaft resistance of the pile groups with $3b$ and $6b$ pile spacing is

30.67 kPa and 30.32 kPa, respectively, with little change. Therefore, pile spacing can change the distribution pattern of surface friction, but it has little effect on the overall pile surface friction.

5.2.2. Pile Group Effect. Pile group effect is often quantified by the group efficiency [51]. The comparisons of group efficiency with different pile spacing are shown in Table 3; when $S = 25$ mm, the group efficiency of shaft resistance and tip resistance and composite group efficiency of the shaft and tip resistance are η_s , η_p , and η_{sp} , respectively [52]. In dense sand, the shaft resistance increases with the settlement hardening of pile groups, and the group efficiency of shaft resistance is greater than 1.0, and the pile group with $6b$ pile spacing is higher. For the pile group with $3b$ pile spacing, due to the reverse lateral soil deformation beneath the tip of adjacent piles, the tip resistance is enhanced, and the group efficiency of tip resistance is greater than 1.0. However, for the pile group with $6b$ pile spacing, the group efficiency of tip resistance is less than 1.0. The composite group efficiency of shaft resistance and tip

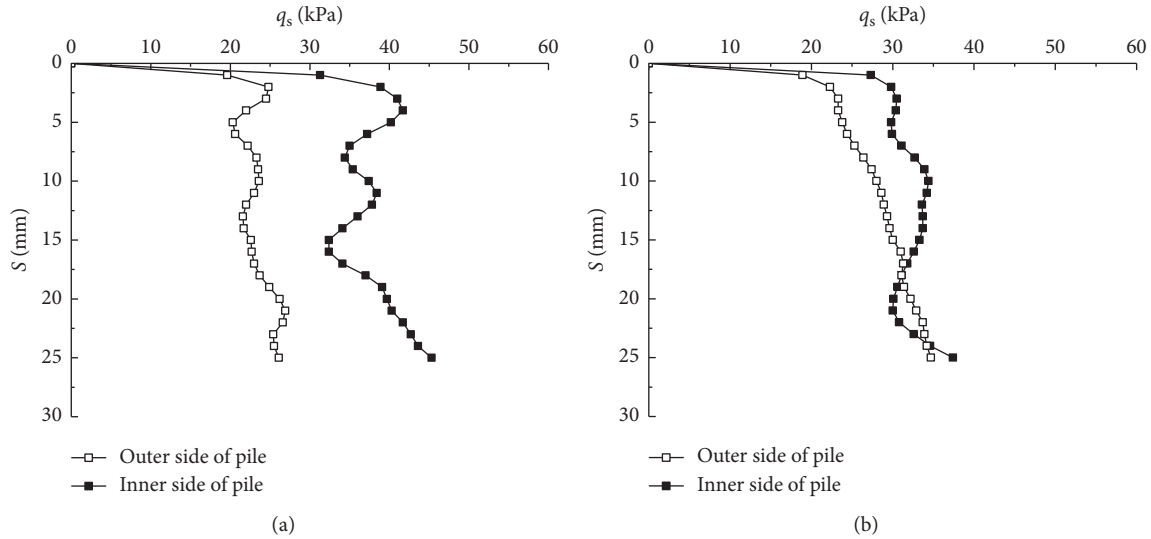


FIGURE 16: The pile shaft resistance-settlement curves. (a) $3b$ pile spacing. (b) $6b$ pile spacing.

TABLE 3: Comparison of group efficiency.

Pile group	η_s	η_p	η_{sp}
$3b$ pile spacing	1.01	1.19	1.05
$6b$ pile spacing	1.13	0.94	1.09

resistance is greater than 1.0 for the pile group with different pile spacing. If the cap effect is taken into account, the group efficiency will be larger. In order to facilitate the design, the Chinese pile foundation code stipulates that when the pile spacing exceeds $3b$, the group efficiency is not taken into account; the analysis results validate the rationality of this code and show that the pile group with $6b$ pile spacing has higher safety reserve.

5.2.3. Contact Force Chain. The distribution of the contact force chain is shown in Figure 17, which is closely related to the pile-sand interaction. The width of the contact force chain represents the size of the contact force. The larger value of contact force in the pile group with $3b$ pile spacing is mainly distributed at the edge of the cap, the inner surface of the piles, and near the pile tip, while the larger value of contact force in the pile group with $6b$ pile spacing is mainly distributed beneath the cap and the pile tip. In addition, the sand contact force near the pile tip of the pile group with $3b$ pile spacing is larger than that of $6b$ pile spacing, but the contact force beneath the cap is smaller than that of the pile group with $6b$ pile spacing.

5.2.4. Vertical Sand Stress. The development of sand vertical stress under the cap at different settlement stages is shown in Figure 18. At the initial stage of settlement, for the pile group with $3b$ pile spacing, the stress level of the sand under the cap is low and mainly concentrated in the sand between piles,

which indicates that the development of the bearing capacity of the sand under the cap lags behind. With the increase in the settlement, the vertical stress of sand increases continuously. Especially, the vertical stress of sand under the central line of the pile group with $6b$ pile spacing increases rapidly, and it still keeps increasing after the settlement S exceeds 15 mm. The sand under the central line of the pile group with $3b$ pile spacing has reached the limit state where the settlement $S = 15$ mm, but the vertical stress at the corner of the cap begins to jump, and the stress concentration is obvious. In the final settlement stage, the average vertical stress under the cap with $3b$ and $6b$ pile spacing is 260 kPa and 291 kPa, respectively, which indicates that the bearing capacity of the sand under the cap with $6b$ pile spacing is fully developed.

The vertical stress curves of the sand inside, outside, and under the pile tip are shown in Figure 19. For the pile group with $3b$ pile spacing, due to the obvious stress superposition beneath the pile tip, the vertical stress in the inner side of the pile tip is obviously greater than the outer side. In the middle and later stages of the settlement, due to the increase in penetration displacement, the vertical stress of the sand at the inner side and under the pile tip continues to grow rapidly. In the final settlement stage, the vertical stress of the sand under the pile tip is 328 kPa, while that of the pile group with $6b$ pile spacing is 124 kPa, which shows that the small pile spacing is beneficial to the exertion of the tip resistance.

For the pile group with $6b$ pile spacing, the vertical stress of the sand at the inner side of the pile tip is slightly higher than the outer side, which may be affected by the stress diffusion from the sand under the cap to the plane of the pile tip. In the middle and later stages of the settlement, the vertical stress of the sand under the pile tip keeps increasing slowly, while the vertical stress of the sand inside and outside the pile tip remains basically unchanged, which indicates that the bearing capacity of the sand beneath the pile tip has been brought into play earlier.

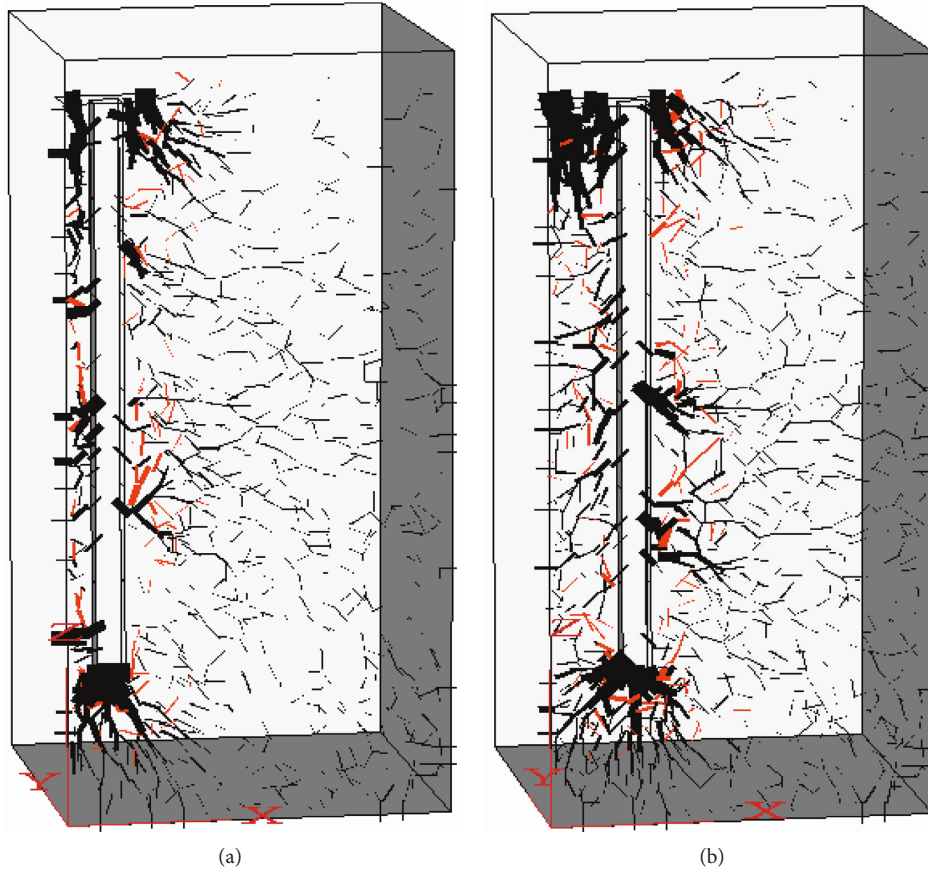


FIGURE 17: Force chains between the pile and sand. (a) $3b$ pile spacing. (b) $6b$ pile spacing.

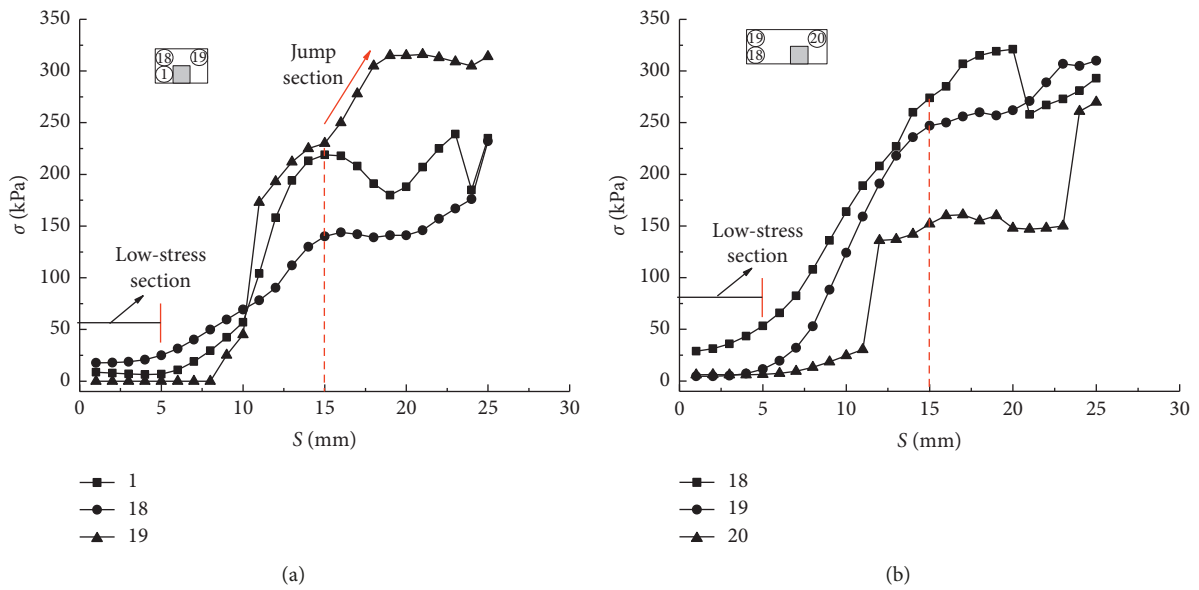


FIGURE 18: Sand vertical stress distribution beneath the cap. (a) $3b$ pile spacing. (b) $6b$ pile spacing.

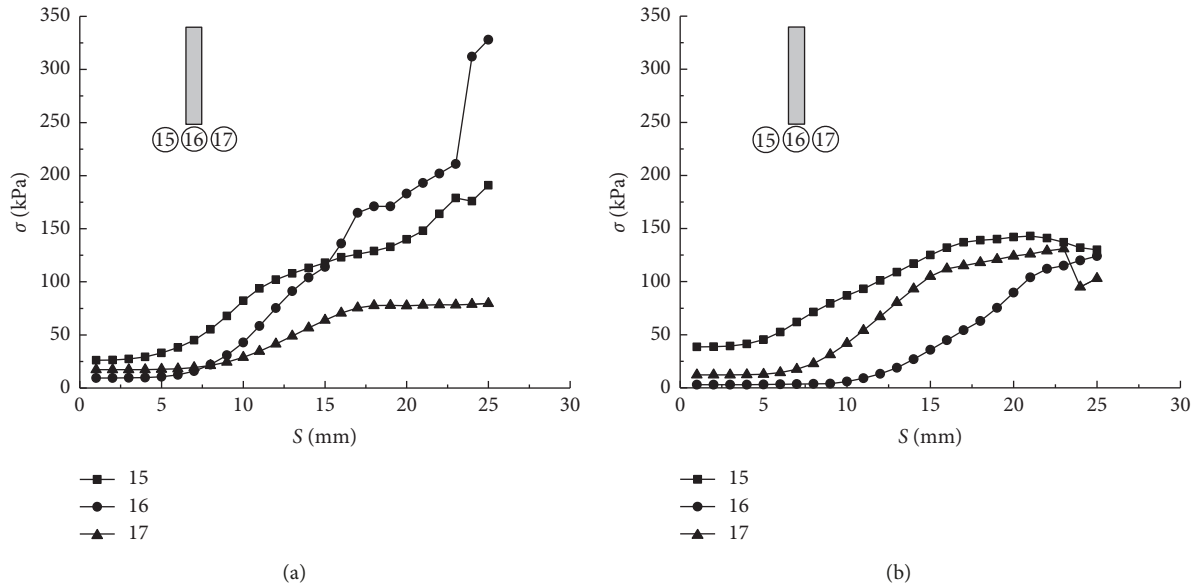


FIGURE 19: Sand vertical stress distribution beneath the pile tip. (a) $3b$ pile spacing. (b) $6b$ pile spacing.

6. Conclusions

Through the visual model test and three-dimensional discrete element numerical simulation, the bearing mechanism of pile groups with conventional pile spacing and large pile spacing is deeply studied. The main conclusions are as follows:

- (1) The change of pile spacing at the initial stage of settlement cannot change the bearing capacity of the pile group. The bearing capacity of the sand beneath the cap with $3b$ pile spacing is hysteretic, and the bearing capacity of the pile group is mainly controlled by piles. The bearing capacity of the cap and piles with $6b$ pile spacing is brought into play synchronously in the middle and later stages of the settlement, and the load-settlement curve has more slow-drop performance.
- (2) Relative displacement exists between the inner side of the pile and sand in the pile group with $3b$ pile spacing. The sand displacement between piles has extended to a certain extent below the pile tip. The sand displacement beneath the pile tip is fan-shaped and partly overlapping, forming a joint shear strain bubble. The sand displacement inside and outside the piles is asymmetrical in the pile group with $6b$ pile spacing, the sand displacement between piles is mainly concentrated in the $4/5L$ range, and the sand displacement beneath the pile tip presents a relatively independent fan-shaped distribution pattern.
- (3) The shaft resistance of the piles is almost exhausted in the initial settlement stage. The shaft resistance of the inner surface of piles with $3b$ pile spacing is about 1.5 times that of the outer surface. The shaft resistance of the inner and outer surface of piles with

$6b$ pile spacing tends to be the same in the final settlement stage, but the average value of the shaft resistance of piles with different pile spacing remains almost unchanged.

- (4) The vertical sand stress beneath the pile tip with $3b$ pile spacing increases rapidly, and it still plays an important role in the later stage of settlement. The vertical sand stress beneath the pile tip with $6b$ pile spacing is significantly lower than that of piles with $3b$ pile spacing.
- (5) The group efficiency of shaft resistance tends to increase with the increase of pile spacing, while the group efficiency of tip resistance tends to decrease. The composite group efficiency of shaft resistance and tip resistance is both greater than 1.0 for these two pile groups, and the pile group with $6b$ pile spacing is larger.

Data Availability

The data used to support the findings of this study are included within the article.

Conflicts of Interest

The authors declare that they have no conflicts of interest regarding the publication of this paper.

Acknowledgments

This work was funded by the National Natural Science Foundation of China (grant no. 51408254), the Six Talent Peak Projects of Jiangsu Province (grant no. JZ-051), and the QingLan Project of Jiangsu Province.

References

- [1] M. F. Randolph, "Science and empiricism in pile foundation design," *Géotechnique*, vol. 53, no. 10, pp. 847–875, 2003.
- [2] B. A. McCabe and B. B. Sheil, "Pile group settlement estimation: suitability of nonlinear interaction factors," *International Journal of Geomechanics*, vol. 15, no. 3, article 04014056, 2015.
- [3] F. Liang, C. Wang, M. Huang, and Y. Wang, "Experimental observations and evaluations of formulae for local scour at pile groups in steady currents," *Marine Georesources & Geotechnology*, vol. 35, no. 2, pp. 245–255, 2017.
- [4] F. S. Tehrani, R. Salgado, and M. Prezzi, "Analysis of axial loading of pile groups in multilayered elastic soil," *International Journal of Geomechanics*, vol. 16, no. 2, article 04015063, 2016.
- [5] D. Park, D. Park, and J. Lee, "Analyzing load response and load sharing behavior of piled rafts installed with driven piles in sands," *Computers and Geotechnics*, vol. 78, pp. 62–71, 2016.
- [6] J. Ju, "Prediction of the settlement for the vertically loaded pile group using 3D finite element analyses," *Marine Georesources & Geotechnology*, vol. 33, no. 3, pp. 264–271, 2015.
- [7] R. C. Chaney, K. R. Demars, S. G. Paikowsky, and F. Xi, "Particle motion tracking utilizing a high-resolution digital CCD camera," *Geotechnical Testing Journal*, vol. 23, no. 1, pp. 123–134, 2000.
- [8] J. M. Zai, G. Jiang, X. D. Wang, X. W. Li, and L. M. He, "Model test on pile-raft foundation interaction under ultimate load," *Chinese Journal of Geotechnical Engineering*, vol. 29, no. 11, pp. 1597–1603, 2007.
- [9] S. A. Hall, M. Bornert, J. Desrues et al., "Discrete and continuum analysis of localised deformation in sand using X-ray μ CT and volumetric digital image correlation," *Géotechnique*, vol. 60, no. 5, pp. 315–322, 2010.
- [10] M. R. Mitchell, R. E. Link, J. Liu, B. Yuan, V. T. Mai, and R. Dimaano, "Optical measurement of sand deformation around a laterally loaded pile," *Journal of Testing & Evaluation*, vol. 39, no. 5, pp. 754–759, 2011.
- [11] J. A. Knappett, S. K. Haigh, and S. P. G. Madabhushi, "Mechanisms of failure for shallow foundations under earthquake loading," *Soil Dynamics and Earthquake Engineering*, vol. 26, no. 2–4, pp. 91–102, 2006.
- [12] T. Sato, K. Onda, and J. Otani, "Development of a new loading test apparatus for microfocus X-ray CT and its application to the investigation of soil behavior surrounding driven open-section piles," *Soils and Foundations*, vol. 58, no. 3, pp. 776–785, 2018.
- [13] F. Yin, Y. Xiao, H. Liu, H. Zhou, and J. Chu, "Experimental investigation on the movement of soil and piles in transparent granular soils," *Geotechnical and Geological Engineering*, vol. 36, no. 2, pp. 783–791, 2017.
- [14] S. Aoyama, W. Mao, S. Goto, and I. Towhata, "Application of advanced procedures to model tests on the subsoil behavior under vertical loading of group pile in sand," *Indian Geotechnical Journal*, vol. 46, no. 1, pp. 64–76, 2016.
- [15] Z. You and Y. Chen, "The use of tactile sensors and PIV analysis for understanding the bearing mechanism of pile groups," *Sensors*, vol. 18, no. 2, p. 476, 2018.
- [16] N. Duan, Y. P. Cheng, and J. W. Liu, "DEM analysis of pile installation effect: comparing a bored and a driven pile," *Granular Matter*, vol. 20, no. 3, pp. 1–16, 2018.
- [17] U. El Shamy and A. Elmekati, "An efficient combined DEM/FEM technique for soil-structure interaction problems," in *Proceedings of the International Foundation Congress and Equipment Expo*, pp. 238–245, Geotechnical Special Publication, Orlando, FL, USA, March 2009.
- [18] J. Zhou, Y. F. Bai, Z. Zhang et al., "Lab model tests and PFC2D modeling of pile groups in sands," *Chinese Journal of Geotechnical Engineering*, vol. 31, no. 8, pp. 1275–1280, 2009.
- [19] N. Sanvitale and E. T. Bowman, "Using PIV to measure granular temperature in saturated unsteady polydisperse granular flows," *Granular Matter*, vol. 18, no. 3, p. 57, 2016.
- [20] M. Ahmed and M. Iskander, "Analysis of tunneling-induced ground movements using transparent soil models," *Journal of Geotechnical and Geoenvironmental Engineering*, vol. 137, no. 5, pp. 525–535, 2011.
- [21] B. Yuan, M. Sun, Y. Wang, L. Zhai, Q. Luo, and X. Zhang, "Full 3D displacement measuring system for 3D displacement field of soil around a laterally loaded pile in transparent soil," *International Journal of Geomechanics*, vol. 19, no. 5, article 04019028, 2019.
- [22] Q. Ni, C. C. Hird, and I. Guymer, "Physical modelling of pile penetration in clay using transparent soil and particle image velocimetry," *Géotechnique*, vol. 60, no. 2, pp. 121–132, 2010.
- [23] B. Yuan, K. Xu, Y. Wang, R. Chen, and Q. Luo, "Investigation of deflection of a laterally loaded pile and soil deformation using the PIV technique," *International Journal of Geomechanics*, vol. 17, no. 6, article 04016138, 2017.
- [24] K. Yamamoto and K. Kusuda, "Failure mechanisms and bearing capacities of reinforced foundations," *Geotextiles and Geomembranes*, vol. 19, no. 3, pp. 127–162, 2001.
- [25] Y. Chen, X. Wang, and Y. She, "Image-based soil deformation measurement in geotechnical model test," *Journal of Civil Architectural & Environmental Engineering*, vol. 34, no. 5, pp. 92–96, 2012.
- [26] J. Liu, M. Liu, and Z. Zhu, "Sand deformation around an uplift plate anchor," *Journal of Geotechnical and Geoenvironmental Engineering*, vol. 138, no. 6, pp. 728–737, 2012.
- [27] J. Cai and G. Zhou, "Research on the failure model of slope foundation based on the evolution feature of displacement field," *China Civil Engineering Journal*, vol. 44, no. S2, pp. 244–248, 2011.
- [28] M. I. Arshad, F. S. Tehrani, M. Prezzi, and R. Salgado, "Experimental study of cone penetration in silica sand using digital image correlation," *Géotechnique*, vol. 64, no. 7, pp. 551–569, 2014.
- [29] M. Houda, O. Jenck, and F. Emeriault, "Physical evidence of the effect of vertical cyclic loading on soil improvement by rigid piles: a small-scale laboratory experiment using digital image correlation," *Acta Geotechnica*, vol. 11, no. 2, pp. 325–346, 2016.
- [30] D. J. White, W. A. Take, and M. D. Bolton, "Soil deformation measurement using particle image velocimetry (PIV) and photogrammetry," *Géotechnique*, vol. 53, no. 7, pp. 619–631, 2003.
- [31] M. D. Bolton, M. W. Gui, J. Garnier et al., "Centrifuge cone penetration tests in sand," *Géotechnique*, vol. 49, no. 4, pp. 543–552, 1999.
- [32] C.-G. Qi, M. Iskander, and M. Omidvar, "Soil deformations during casing jacking and extraction of expanded-shoe piles, using model tests," *Geotechnical and Geological Engineering*, vol. 35, no. 2, pp. 809–826, 2017.
- [33] D. J. White and M. D. Bolton, "Displacement and strain paths during plane-strain model pile installation in sand," *Géotechnique*, vol. 54, no. 6, pp. 375–397, 2004.
- [34] J. Z. Ye, J. Zhou, and B. Han, "Numerical simulation on characteristics of single pile setup by different methods with

- particle flow code based on DEM,” *Chinese Journal of Geotechnical Engineering*, vol. 29, no. 6, pp. 894–900, 2007.
- [35] G. G. Meyerhof, “Influence of roughness of base and ground-water conditions on the ultimate bearing capacity of foundations,” *Géotechnique*, vol. 5, no. 3, pp. 227–242, 1955.
- [36] Y. Geng, H. S. Yu, and G. R. McDowell, “Discrete element modelling of cavity expansion and pressuremeter test,” *Geomechanics and Geoengineering*, vol. 8, no. 3, pp. 179–190, 2013.
- [37] Y. Cui, A. Nouri, D. Chan, and E. Rahmati, “A new approach to DEM simulation of sand production,” *Journal of Petroleum Science and Engineering*, vol. 147, pp. 56–67, 2016.
- [38] W. Zhou, L. F. Yang, G. Ma, K. Xu, Z. Lai, and X. Chang, “DEM modeling of shear bands in crushable and irregularly shaped granular materials,” *Granular Matter*, vol. 19, no. 2, p. 25, 2017.
- [39] O. Jenck, D. Dias, and R. Kastner, “Two-dimensional physical and numerical modeling of a pile-supported earth platform over soft soil,” *Journal of Geotechnical and Geoenvironmental Engineering*, vol. 133, no. 3, pp. 295–305, 2007.
- [40] J. Han, A. Bhandari, and F. Wang, “DEM analysis of stresses and deformations of geogrid-reinforced embankments over piles,” *International Journal of Geomechanics*, vol. 12, no. 4, pp. 340–350, 2012.
- [41] Z. Chen, M. Omidvar, and M. Iskander, “Observations of multi-scale granular kinematics around driven piles in plane strain condition,” *Geotechnical Testing Journal*, vol. 39, no. 5, pp. 827–841, 2016.
- [42] Z. Zhang and Y.-H. Wang, “Three-dimensional DEM simulations of monotonic jacking in sand,” *Granular Matter*, vol. 17, no. 3, pp. 359–376, 2015.
- [43] M. J. Jiang, Y. Xiao, S. L. Chen et al., “Discrete element analysis of bearing mechanism of single pile in sand under vertical load,” *Rock and Soil Mechanics*, vol. 31, no. 2, pp. 366–372, 2010.
- [44] M. Khanal, M. Elmouttie, B. Poulsen, A. Olsson, and D. Adhikary, “Effect of loading rate on sand pile failure: 2D DEM simulation,” *Geotechnical and Geological Engineering*, vol. 35, no. 2, pp. 889–896, 2017.
- [45] S. Lobo-Guerrero and L. E. Vallejo, “Influence of pile shape and pile interaction on the crushable behavior of granular materials around driven piles: DEM analyses,” *Granular Matter*, vol. 9, no. 3-4, pp. 241–250, 2007.
- [46] J. Zhou, Q.-W. Jian, J. Zhang, and J.-J. Guo, “Coupled 3D discrete-continuum numerical modeling of pile penetration in sand,” *Journal of Zhejiang University Science A*, vol. 13, no. 1, pp. 44–55, 2012.
- [47] M. Jiang, Y. Dai, L. Cui, Z. Shen, and X. Wang, “Investigating mechanism of inclined CPT in granular ground using DEM,” *Granular Matter*, vol. 16, no. 5, pp. 785–796, 2014.
- [48] L. Zhang and C. Thornton, “A numerical examination of the direct shear test,” *Géotechnique*, vol. 57, no. 4, pp. 343–354, 2007.
- [49] Y. Chen, A. Deng, A. Wang, and H. Sun, “Performance of screw-shaft pile in sand: model test and DEM simulation,” *Computers and Geotechnics*, vol. 104, pp. 118–130, 2018.
- [50] Y. Chen, X. Wang, Y. She et al., “Macroscopic and mesoscopic working performance of PCC pile subjected to vertical load,” *Chinese Journal of Rock Mechanics and Engineering*, vol. 34, no. 7, pp. 1503–1510, 2015.
- [51] M. M. Sales, M. Prezzi, R. Salgado, Y. S. Choi, and J. Lee, “Load-settlement behaviour of model pile groups in sand under vertical load,” *Journal of Civil Engineering and Management*, vol. 23, no. 8, pp. 1148–1163, 2017.
- [52] F. Han, R. Salgado, M. Prezzi, and J. Lim, “Axial resistance of nondisplacement pile groups in sand,” *Journal of Geotechnical and Geoenvironmental Engineering*, vol. 145, no. 7, article 04019027, 2019.



Hindawi

Submit your manuscripts at
www.hindawi.com

